RESEARCH ARTICLE

Majun SONG, Sheng GUO, Anderson S. OLIVEIRA, Xiangyang WANG, Haibo QU

Design method and verification of a hybrid prosthetic mechanism with energy-damper clutchable device for transfemoral amputees

Abstract Transfemoral amputees (TAs) have difficulty in mobility during walking, such as restricted movement of lower extremity and body instability, yet few transfemoral prostheses have explored human-like multiple motion characteristics by simple structures to fit the kinesiology, biomechanics, and stability of human lower extremity. In this work, the configurations of transfemoral prosthetic mechanism are synthesized in terms of human lower-extremity kinesiology. A hybrid transfemoral prosthetic (HTP) mechanism with multigait functions is proposed to recover the gait functions of TAs. The kinematic and mechanical performances of the designed parallel mechanism are analyzed to verify their feasibility in transfemoral prosthetic mechanism. Inspired by motion–energy coupling relationship of the knee, a wearable energy-damper clutched device that can provide energy in knee stance flexion to facilitate the leg off from the ground and can impede the leg's swing velocity for the next stance phase is proposed. Its co-operation with the springs in the prismatic pairs enables the prosthetic mechanism to have the energy recycling ability under the gait rhythm of the knee joint. Results demonstrate that the designed HTP mechanism can replace the motion functions of the knee and ankle to realize its multimode gait and effectively decrease the peak power of actuators from 94.74 to 137.05 W while maintaining a good mechanical adaptive stability.

Keywords hybrid transfemoral prosthetic mechanism, energy recycling, wearable mechanical clutched device, mechanical adaptive stability

Majun SONG, Sheng GUO (✉), Xiangyang WANG, Haibo QU
School of Mechanical, Electronic and Control Engineering, Beijing Jiaotong University, Beijing 100044, China
E-mail: shguo@bjtu.edu.cn

Anderson S. OLIVEIRA
Department of Materials and Production, Aalborg University, Aalborg 9220, Denmark

1   Introduction

Nowadays, lower-extremity prostheses are increasingly used worldwide, especially for individuals after above-knee amputation due to traffic accidents, diabetes mellitus, and dysvascular disease [1]. Transfemoral amputees (TAs) always lose their ability to move and have a higher risk of falling, which leads to a life of poor quality, because the lower extremities play the main functions in human locomotion and body support. Therefore, robotic prostheses with human-like performances are needed to restore the lost motion function of TAs [2].

Thanks to the continuous development of robot technology, powered lower limb robotic prostheses, have been extensively studied and manufactured for TAs in recent years. They can effectively resolve the shortcomings of traditional prostheses such as high metabolic consumption of the prosthetic wearers, high gait coordination error, poor wearability, and low degree of freedom. Sup et al. [3] proposed a gait controller in a designed powered transfemoral prosthesis, which uses passive impedance to coordinate the prosthetic motion. Yang and Kim [4] designed an above-knee powered prosthetic leg and an algorithm to achieve suitable gait recognition synchronized with the motion of the prosthetic wearer. Lenzi et al. [5] designed a lightweight robotic lower limb prosthesis, which is actuated by a novel hybrid control system and has passive and active operation modes. Lawson et al. [6] proposed a ground-adaptive standing controller in a designed knee–ankle prosthesis. This controller can improve the stability of TAs when wearing this prosthesis. These prostheses can help TAs recover the human-like motion function of the

knee and ankle as well as reduce their metabolic consumption during walking. However, existing knee–ankle prostheses have a limited motion pattern such that the knee and ankle can only rotate in the sagittal plane. They have insufficient carrying capacity due to serial open-loop structures. Moreover, knee joints have frequent acceleration and deceleration motion during a gait cycle. Therefore, linear elastic devices are not suitable. Foot external rotation and varus–valgus rotation are also required because knee flexion–extension and ankle plantarflexion–dorsiflexion of the transfemoral prosthetic mechanism are not sufficient to cope with walking task in complex terrain. To realize the multiple degrees-of-freedom (DoFs) motion function of prostheses, several scholars try to add more transmissions in their prostheses, which make them heavier and structurally complex. Parallel mechanisms (PMs) [7,8] have the advantages of simple structure, multi-DoF characteristics, large carrying capacity, and high motion precision, which have been widely used in industrial engineering. Generally, the number of DoFs determines the number of actuators in PMs, but multi-DoF motion characteristics can be realized by fewer actuators for the under actuation PMs [9]. The human lower extremity is a multi-DoF motion system. Hence, sufficient carrying capacity is required to support the weight of the human body, and PMs are suitable for the development of novel lower-extremity prostheses. To our knowledge, PMs have not been used in the development of transfemoral prosthetic mechanisms.

Combined with the designed ankle–foot prosthetic mechanism presented in our previous work [10], a hybrid transfemoral prosthetic (HTP) mechanism is proposed. According to configuration synthesis theory, a class of PM configurations with rotational three-DoF function is synthesized and employed to mimic the natural motion of the knee and ankle, that is, knee flexion–extension, knee internal–external rotation, and ankle varus–valgus rotation. A wearable energy-damper clutched (WEDC) device for the knee joint is also proposed in terms of the biomechanical difference between the amputated and sound legs of TAs, which can reduce the energy consumption of TAs, facilitate the knee stance flexion to help the HTP mechanism leave the ground, and impede the leg's swing (SW) velocity for the next heel-strike (HS) of gait.

The paper is organized as follows. Section 2 describes the prosthetic configuration synthesis for TAs in terms of the kinesiology of human lower extremity, discusses the design method of PMs with three-DoF rotational function proposed by Lie group theory, and presents the conceptual design of HTP mechanism with WEDC device. Section 3 investigates the feasibility of the selected PM based on the analysis of its kinematic and mechanical performances. Section 4 shows the simulation results of the designed HTP mechanism. Finally, Section 5 draws the conclusions.

2 Configuration synthesis of shank structure

2.1 Human lower extremity kinesiology

For existing transfemoral prostheses, the simple transmission mechanism can only help TAs meet the movement in sagittal plane, that is, anatomically [11] defined knee flexion–extension and ankle dorsiflexion–plantarflexion. However, medical research has shown that the foot movement in the coronal and horizontal planes is essential, which will provide the lower extremity the adaptive ability when walking on different road conditions. Thus, this work aims to propose a novel structure of transfemoral prosthetic mechanism that also considers knee internal–external rotation and ankle varus–valgus rotation.

In this work, a group of eight healthy subjects with a height range of 1.70−1.85 m and a weight range of 70−85 kg is selected, and the motion characteristics of the lower extremity can be obtained by three-dimensional (3D) motion capturing system of the subjects with constant walking velocity, as listed in Table 1.

Generally, the gait cycle when a human is walking in the sagittal plane can be divided into six phases, namely, HS, foot-flat (FF), heel-off (HO), toe-off I (TO-I), toe-off II (TO-II), and SW, as shown in the upper picture of Fig. 1(a). Relatively, the gait curves of the knee and ankle versus gait period can also be fitted by the experimental data, as shown in the lower picture of Fig. 1(a).

Given the motion characteristics of the knee and ankle, a prosthetic mechanism with three-DoF motion characteristics that can generate human-like motion and joint stiffness of the knee and ankle is anticipated, as shown in Fig. 1(b). For the preliminary hypothesis, four possible configurations used in transfemoral prosthetic mechanism are motivated, as shown in Fig. 2. Therefore, the one-DoF rotary mechanism or special rotary mechanism with

Table 1   Lower extremity kinesiology of eight normal subjects

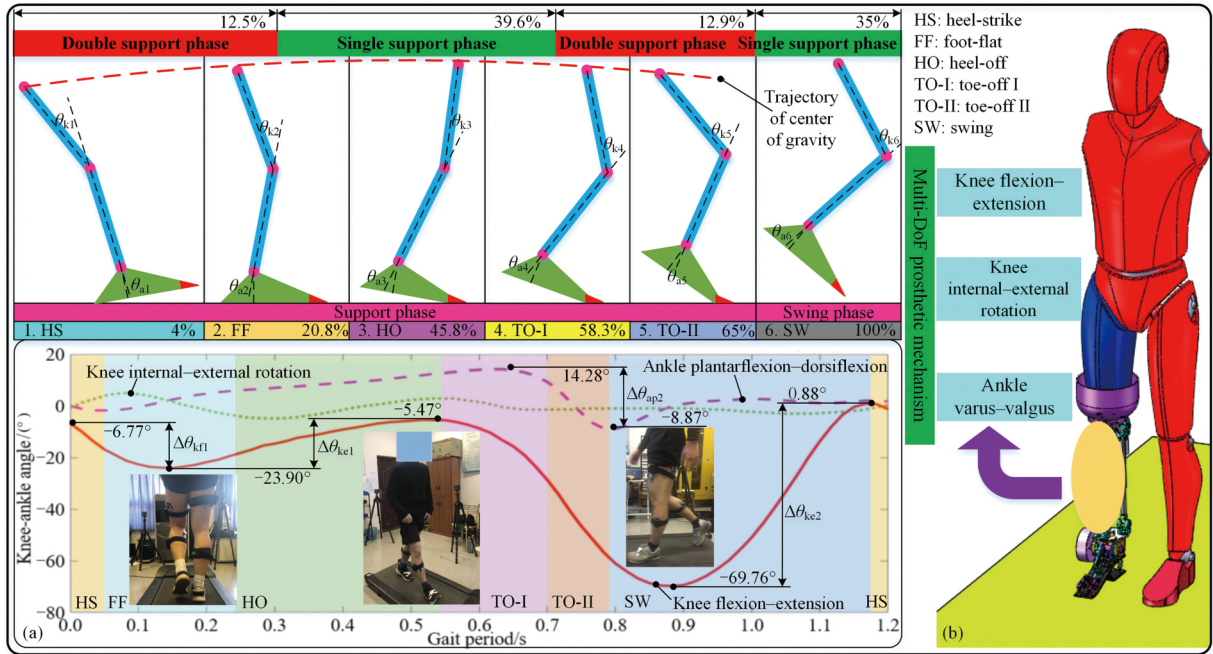| Category	Represent	Value
Human body characteristics	Average height	1.75 m
	Average weight	76.1 kg
Motion characteristics	Walking velocity	1.3 m/s
	Ankle plantarflexion–dorsiflexion	−8.87°–14.28°
	Ankle varus–valgus rotation	−12.45°–1.02°
	Knee flexion–extension	−69.76°–0.88°
	Knee internal–external rotation	−14.25°–14.25°

Fig. 1 Kinesiology of human knee and ankle versus time. (a) Gait experiments and results; (b) predicted human-machine model.
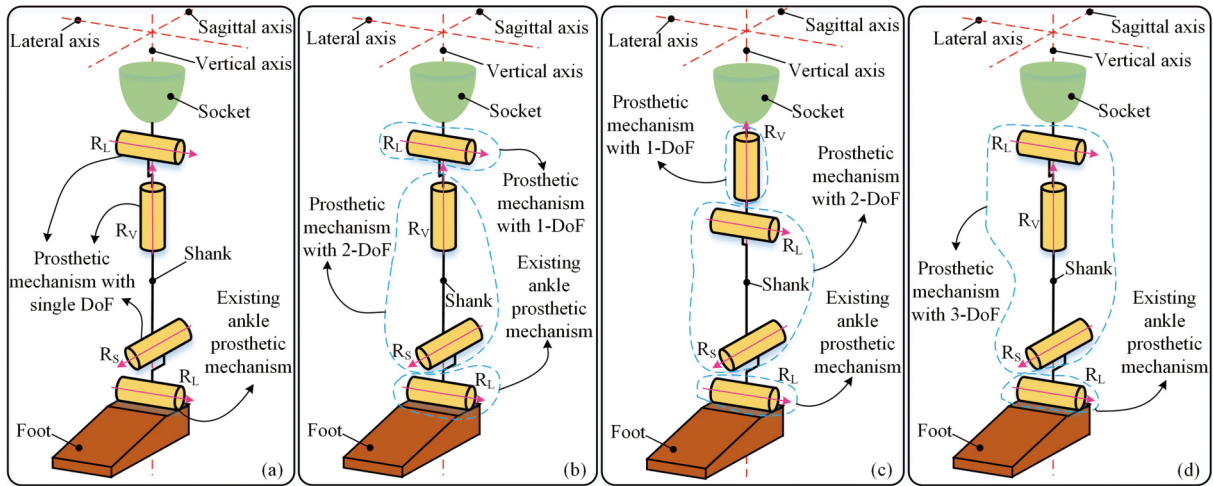

Fig. 2 Configuration synthesis in transfemoral prosthetic mechanism. (a) Serial mechanism; (b) hybrid mechanism I: two 1-DoF mechanisms and a 2-DoF mechanism; (c) hybrid mechanism II: two 1-DoF mechanisms and a 2-DoF mechanism; and (d) hybrid mechanism: a 3-DoF mechanism and a 1-DoF mechanism.

multiple DoFs can be adopted to design the prosthetic mechanism with three-DoF motion characteristics in the transfemoral mechanism except ankle plantarflexion–dorsiflexion.

A proper configuration should avoid overweight at its distal end because it will lead to its great inertia, poor kinematic dexterity, and dynamic response. Based on this, a prosthetic mechanism with three-DoF motion characteristics can be selected as the reasonable configuration in transfemoral prosthetic mechanism, and it is a series–parallel hybrid prosthetic mechanism, as shown in Fig. 2(d).

2.2 Theoretical design of three-DoF PMs

2.2.1 Design principles

To design the prosthetic mechanism with three-DoF motion characteristics, four design principles listed below must be followed in terms of the kinesiology of human lower extremity. A special mechanism is motivated, and its fundamental motion characteristic schematic diagram is represented in Fig. 3.

(1) To mimic the contraction and extension of the calf gastrocnemius better, a prismatic pair with linear spring,
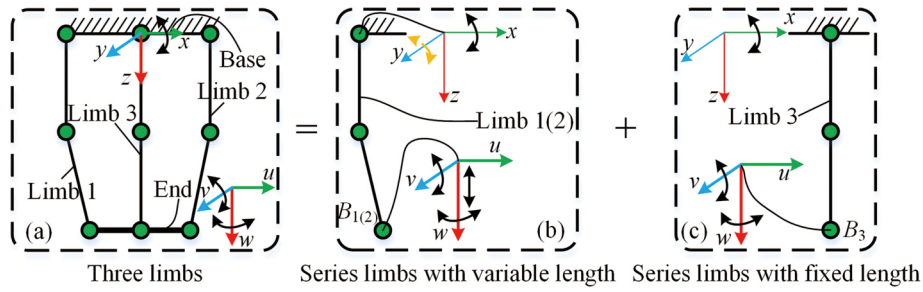
Fig. 3 3D spatial motion of free ends of each limb: (a) 3R motion, (b) 3R1T/3R1T-T motion, and (c) 3R motion.

whose direction is along the limbs, is adopted in the middle pair of the first and second limbs. To replace the calf, a fixed-length limb, which is equal to the shank length, must be presented. Thus, only the revolute pair, whose direction is along the limb, can be used in the middle pair of the third limb.

(2) To improve gait stability, the configuration of the proposed mechanism should be symmetrical. The first and second limbs in this mechanism should be the same and symmetrical in the sagittal plane.

(3) To achieve the flexion–extension of the knee with a large rotational angle, each limb has a revolute pair fixed on the fixed base, and their axes are parallel to the human lateral axis. To achieve the varus–valgus of the ankle with a small rotational angle, each limb has a revolute pair that is fixed on the moving platform, and their axes are parallel to the human sagittal axis.

(4) To ensure stability, each limb has at most a prismatic pair, and it cannot be installed on the fixed base and moving platform.

2.2.2   Configuration synthesis of three-DoF mechanism

As mentioned above, Lie group theory, which is a group with differential manifold first proposed by Sophus Lie in the study of symmetry of differential equations [12,13], is used to synthesize the reasonable limbs. Finally, the required prosthetic mechanism can be obtained by intersection operation. Based on Lie group theory, the motion characteristics of the proposed mechanism can be expressed.

$$D_m = [R(O, x) \cdot R(O, y) \cdot R(O, z)] = L_{m1} \cap L_{m2} \cap L_{m3}, \quad (1)$$

where $R(O, x)$, $R(O, y)$, and $R(O, z)$ are the rotational ability of the moving platform around the x, y, and z axes, that is, anatomically the lateral axis, sagittal axis, and vertical axis, respectively, L_{m1}, L_{m2}, and L_{m3} denote three limbs in PM that can be built by the generator of displacement subgroups in terms of Lie group theory, L_{m1} and L_{m2} are the same limbs based on the second design principle, D_m is the motion characteristic of the moving platform, and $\cap$ is the intersection operation.

Figure 3 shows that the motion characteristics of three DoFs are considered in the proposed mechanism, and both ends of the three limbs should connect with the base and end components by a revolute pair, which are parallel to the anatomical lateral and sagittal axes, respectively. Therefore, the generators of the middle kinematic pairs and the equivalent kinematic limbs can be obtained in terms of the Lie subgroups, as shown in Tables 2 and 3.

In Tables 2 and 3, $R(N, x)$, $R(N, y)$, and $R(N, z)$ denote that the axes of the revolute pairs go through N, and their directions are parallel to the x, y, and z axes, respectively. $T(x)$, $T(y)$, and $T(z)$ represent the prismatic pairs sliding along the x, y, and z axes, respectively.

Based on the configurations of L_{m1}, L_{m2}, and L_{m3}, the

Table 2   Configuration of L_{m1} and L_{m2} based on Lie group theory

Screw	Middle generator expression	Equivalent kinematic limb
3	$T(z)$	$^xR^zP^yR$
4	$[R(N, z) \cdot T(z)]$	$^xR^zC^yR$, $^xR[^zR^zP]^yR$, $^{xz}U^zP^yR$, $^xR^zP^zyU$
5	$[R(N_1, x) \cdot T(z) \cdot R(N, z)]$ $[T(y) \cdot R(N_1, x) \cdot R(N, z)]$	$^xR[^xR^zP^zR]^yR$, $^xR[^xR^zC]^yR$, $^xR[^xR^zP]^{zy}U$, $^xR^zP^{xyz}S$, $^xR[^xR^zC]^yR$, $^xR^zP^zR^{xy}U$, $^xR^zC^{xy}U$, $^xR[^{xz}]U^zP]^yR$, $^{xz}U[^xR^zP]^yR$, $^{xz}U^zP^{xy}U$, $^xR[^yP^xR^zR]^yR$, $^xR[^yP^{[xz]}U]^yR$, $^xR[^yP^xR]^{zy}U$, $^xR^yP^{xyz}S$, $^xR[^zR^yP]^{zy}U$, $^{xz}U[^yP^xR]^yR$, $^{xz}U^yP^{xy}U$
	$[R(N, z) \cdot R(N_1, y) \cdot T(z)]$ $[R(N, z) \cdot T(x) \cdot R(N_1, y)]$	$^xR[^zR^yR^zP]^yR$, $^xR[^{[zy]}U^zP]^yR$, $^xR[^zC^yR]^yR$, $^xR[^yR^zP]^{zy}U$, $^{xy}U[^zR^zP]^yR$, $^{xy}U^zC^yR$, $^{xy}U^zP^{zy}U$, $^{xz}U[^yR^zP]^yR$, $^{xyz}S^zP^yR$, $^xR[^zR^xP^yR]^yR$, $^xR[^{[zy]}U^xP]^yR$, $^xR[^xP^yR]^{zy}U$, $^{xy}U^xP^{zy}U$, $^{xy}U[^zR^xP]^yR$, $^{xyz}S^xP^yR$, $^{xz}U[^xP^yR]^yR$
6	$[R(N, z) \cdot R(N_1, z) \cdot R(N_2, z) \cdot T(z)]$ $[R(N, z) \cdot R(N_1, x) \cdot R(N_2, y) \cdot T(z)]$	$^xR[^zR^zR^zR^zP]^yR$, $^xR[^zR^zR^zC]^yR$, $^{xz}U^zC^{zy}U$, $^zU[^zR^zP]^{zy}U$, $^xR[^zR^xR^yR^zP]^yR$, $^{xy}U^zC^{xy}U$, $^xR[^zC^xR^yR]^yR$

limb of $^{xy}U^zC^{xy}U$ can be selected as the configuration of the first and second limbs, and $^{x}R^zR^yR$ can be defined as the configuration of the third limb. The proposed mechanism is 2-UCU/RRR PM, which can replace the flexion–extension, intension–extension of the knee, and varus–valgus of the ankle, as shown in Fig. 4.

2.3 Conceptual design of HTP mechanism

2.3.1 HTP mechanism with WEDC device

Finally, the HTP mechanism with WEDC device can be designed, as shown in Fig. 5(a). It mainly consists of an designed ankle–foot prosthetic mechanism, a 2-UCU/RRR PM, and a WEDC device used in the knee, as shown in Figs. 5(b)–5(d). The ankle–foot prosthetic mechanism [10] has the motion characteristic of dorsiflexion–plantarflexion and is mainly composed of motor module, mounting base, spring cushion system, series spring device of three-loop mechanism, parallel spring device of compliant crank slider mechanism, circular adaptive block, and carbon fiber prosthetic foot, as shown in Fig. 5(d). Especially, the series spring device can efficiently promote the movement of the ankle–foot prosthetic mechanism with human-like ankle stiffness, and the parallel spring device including a flexible hinge as toe joint provides greater energy for the ankle–foot prosthetic mechanism at end of the toe-off phase to reduce the peak power requirement of motor. Moreover, self-adaptive analysis indicates that the circular adaptive block, which has not been adopted in existing transtibial prostheses, has a better mechanical self-adaptability. In this work, the feasibility of 2-UCU/RRR PM with respect

to the kinematic functions and mechanical performances are analyzed and verified.

Different from existing transfemoral prostheses that only have the rotational characteristics of the knee and ankle in the sagittal plane, the designed HTP mechanism has multi-DoF motion characteristics under a simple structure, that is, it also has the motion of knee internal–external rotation and ankle varus–valgus rotation besides knee flexion–extension and ankle dorsiflexion–

Table 3 Configuration of L_{m3} based on Lie group theory.

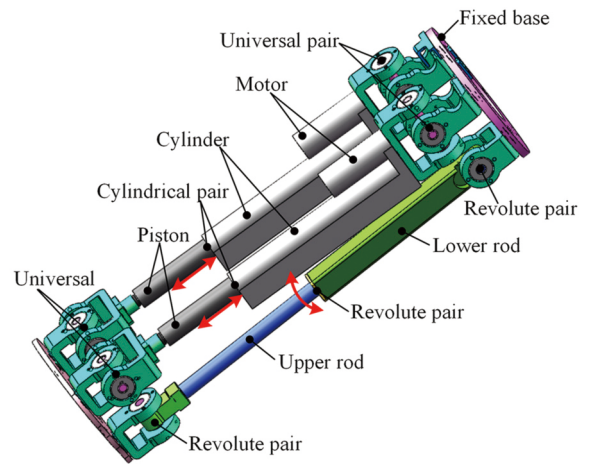| Screws	Middle generator expression	Equivalent kinematic limb
3	$R(N, z)$	$^{x}R^zR^yR$, $^{xz}U^yR$, $^{x}R^zyU$
4	$[T(x)\cdot R(N, z)]$	$^{x}R[^{x}P^zR]^yR$, $^{x}R^xP^{zy}U$, $^{xz}U^xP^yR$,
	$[R(N, z)\cdot T(y)]$	$^{x}R[^zR^yP]^yR$, $^{xz}U^yP^yR$, $^{x}R^yP^{zy}U$, $^{x}R^zR^{xy}U$

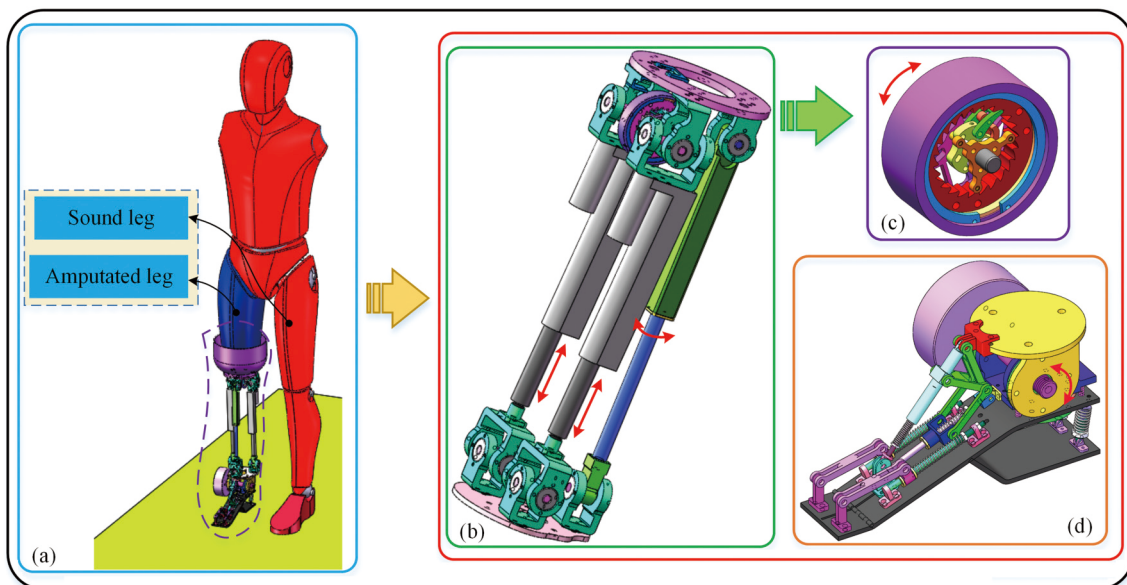**Fig. 4** 2-UCU/RRR PM with 3-DoF pure rotation.

Fig. 5 Prototype of HTP mechanism. (a) Human-machine model with transfemoral prosthetic mechanism; (b) 2-UCU/RRR parallel mechanism; (c) energy-damper clutched device; (d) ankle-foot prosthetic mechanism.

plantarflexion. The HTP mechanism can help TAs restore their lost movement ability and adapt to different terrain.

2.3.2   Wearable energy-damper clutched device

A. Structural design

The designed WEDC device works like a mechanical unidirectional clutch, which is different from the existing linear clutched energy devices used in prosthetic mechanisms, as shown in Fig. 5(c).

The exploded views of the WEDC device are presented in Fig. 6. The fixed frame is installed on the fixed base of 2-UCU/RRR PM, the torsion spring and fixed frame are connected by bolts in their central three holes, and it is connected with the unidirectional ratchet by six bolts at their boundary. The push rod is tangent to the teeth of the unidirectional ratchet during knee flexion, and the clutched device will not work, but it will rotate against the teeth of unidirectional ratchet with the rotation of the joint axis to promote the planar rotation of the torsion spring during knee extension because the joint axis is coaxial with the prosthetic knee axis connected by couplings.

B. Structural optimization of torsional spring

To generate the required moment and power for the HTP mechanism when the knee extends $\Delta\theta_{ke}$ of extension, the topology optimization method is used in the development of the customized torsion spring. According to the solid isotropic material penalization [14–16], the numerical optimal model of torsion spring can be built.

$$
\begin{aligned}
&\text{find}\rho_j \ (j = 1, 2, ..., N), \\
&\max C(\rho_j,t) = \int T(\rho_j,t)\dot{\theta}(t)\mathrm{d}t, \\
&\text{s.t.}\ \ \theta(t) \geqslant [\Delta\theta_{ke}(t)], \\
&\qquad T(\rho_j,t) \geqslant [\Delta M_{ph2} + \Delta M_{pk2}], \\
&\qquad V = \int \rho_j \mathrm{d}\Omega \leqslant V^*, \\
&\qquad 0 < \rho_{min} \leqslant \rho_j \leqslant 1,
\end{aligned}
\tag{2}
$$

where ρ_j is the design variable, which indicates the artificial material density of 60Si2Mn-A, (ρ_j, t) of energy function is the optimization objective, $\theta(t)$ is the knee extension angle, which indicates that the optimized torsion spring can rotate at least $\Delta\theta_{ke}$, $\dot{\theta}(t)$ is the angular acceleration, $T(\rho_j, t)$ is the knee moment generated by optimized torsion spring, which is referred to the biomechanical analysis results of Fig. A1 in Appendix, ΔM_{ph2} is the extra hip extensor moment which endured by the TAs, ΔM_{pk2} is the lack of knee flexor moment in the prosthetic system, V and V^* are the optimized and desired volumes, respectively, Ω is the design area, and ρ_{min} is the minimum density of the element, which is set to avoid the singularity of the optimization.
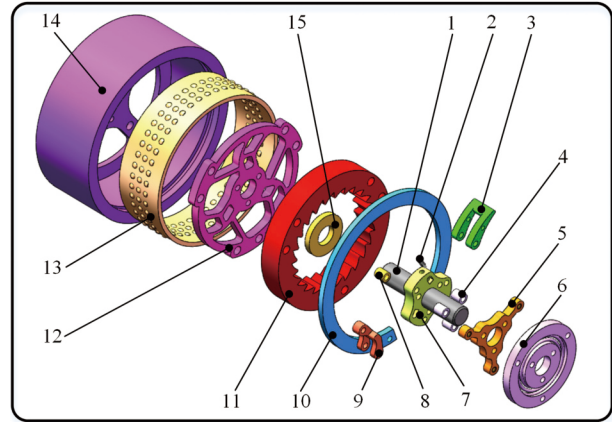
As described above, the working principle of the

Fig. 6 Explosion diagram of WEDC device. 1–joint axis (coaxial with prosthetic knee), 2–spring, 3–push rod, 4–spacer bush B, 5–rotational frame, 6–preload torsion spring, 7–rotational wheel, 8–spacer bush A, 9–movable push rod, 10–baffle ring, 11–unidirectional ratchet, 12–customized torsion spring, 13–oilless bearing, 14–fixed frame, and 15–spacer bush.

WEDC device can be clearly displayed through the planar configuration, as shown in Figs. 7(a)–7(b). In particular, the connectivity relationship of the torsional spring with the fixed frame and ratchet can also be explained by the rear view of the WEDC device in Fig. 7(b). The torsional spring in Fig. 7(b) is an imaginary structure that facilitates readers to comprehend its working condition. The loads–boundary conditions of the customized torsional spring in the WEDC device can be equivalent in terms of its actual working condition, as shown in Fig. 7(c).

The optimality criteria method [17,18] is adopted to solve its optimization problem, and the optimal result can be obtained, as shown in Figs. 7(d)–7(e). Figure 7(d) shows that the material density in the blue area is approximately equal to 0, which means that the existence of this area does not affect the mechanical performance in the WEDC device, and this area can be removed. On the contrary, the material density in the red area is approximately equal to 1, which means that the red area is the force transmission path, and the material in this area must be retained. Therefore, the layout of the red area is the conceptual structure of customized torsion spring, and the optimal configuration of customized torsion spring can be developed by taking its optimization result as the design reference, which is different from the existing torsion springs.

Static analysis is implemented, which verifies the feasibility of the optimal configuration of the customized torsion spring in the WEDC device, as shown in Fig. 7(e). The maximum rotation displacement of the customized torsion spring is approximately 0.9819 rad, which is approximately 56.3°, that is, it can generate the desired mechanical performance without affecting the knee flexion–extension.
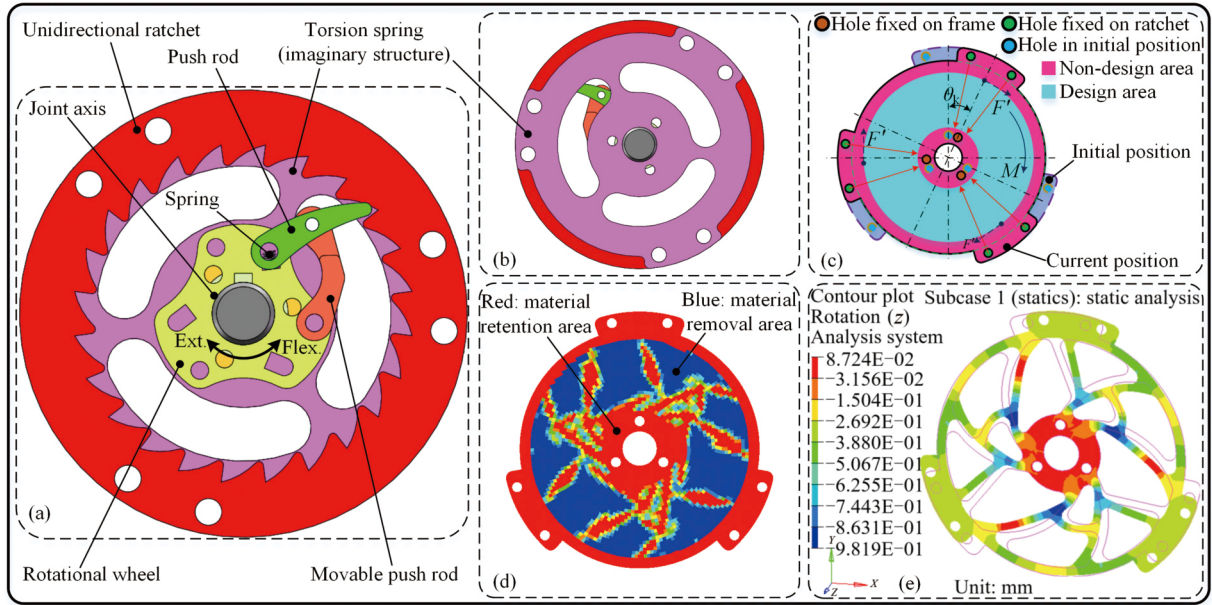
Fig. 7 Schematic diagram of WEDC device: (a) structural schematic diagram of WEDC device, (b) unidirectional ratchet with torsion spring, the working principle of customized torsional spring is equivalent to the traditional torsional spring of the picture, (c) definitions of design area, boundary conditions and load of the torsion spring is described, (d) optimal configuration of torsion spring based on topology optimization, and (e) simulation verification of the customized torsion spring. Ext.: extension, Flex.: flexion.

3 Modelling and performance analysis

3.1 Performance verification of 2-UCU/RRR PM

3.1.1 Movement kinematic verification

The diagram of the 2-UCU/RRR PM in HTP mechanism is described in Fig. 8. The fixed base $\Delta A_1 A_2 A_3$ and moving platform $\Delta B_1 B_2 B_3$ are equilateral triangles, $|A_1 A_2| = |A_2 A_3| = |A_1 A_3| = 2a$ and $|B_1 B_2| = |B_2 B_3| = |B_1 B_3| = 2b$ (a and b are real constant), respectively. O–xyz is a

fixed frame, and its origin is point O located at the center of $A_1 A_2$, P–$x_1 y_1 z_1$ is a moving frame, its origin is point P located at the center of $B_1 B_2$, and their axes comply with the right-hand rule. The revolute pair is installed at the center of $\Delta B_1 B_2 B_3$ and $AP = b$. A is the origin of A–$x_2 y_2 z_2$, and z_2 is along the axis of the revolute pair. P–$x_1 y_1 z_1$ is rotated around y_1 axis for $-90°$ and translated along the y_1 axis for the distance of AP; thus, A–$x_2 y_2 z_2$ can be obtained.

To verify its movement, screw theory [19,20] is often used. Thus, the kinematic screws of three limbs of 2-UCU/RRR PM can be represented.

$$
\begin{cases}
\pmb{\$}_{11} = [1, 0, 0, 0, 0, 0], \\
\pmb{\$}_{12} = [0, 1, 0, 0, 0, 1], \\
\pmb{\$}_{13} = [l_1, 0, n_1, 0, -1, 0], \\
\pmb{\$}_{14} = [0, 0, 0, l_2, 0, n_2], \\
\pmb{\$}_{15} = [1, 0, 0, 0, 1, 0], \\
\pmb{\$}_{16} = [0, 1, 0, l_3, 0, n_3],
\end{cases}
\begin{cases}
\pmb{\$}_{21} = [1, 0, 0, 0, 0, 0], \\
\pmb{\$}_{22} = [0, 1, 0, 0, 0, -1], \\
\pmb{\$}_{23} = [-l_1, 0, n_1, 0, 1, 0], \\
\pmb{\$}_{24} = [0, 0, 0, -l_2, 0, n_2], \\
\pmb{\$}_{25} = [1, 0, 0, 0, -1, 0], \\
\pmb{\$}_{26} = [0, 1, 0, l_3, 0, -n_3],
\end{cases}
\begin{cases}
\pmb{\$}_{31} = [1, 0, 0, 0, 0, 1], \\
\pmb{\$}_{32} = [0, -m_1, n_1, 0, 0, 0], \\
\pmb{\$}_{33} = [0, 1, 0, 1, 0, 0].
\end{cases}
\tag{3}
$$

Their constraint screws $\pmb{\$}_{31r}$, $\pmb{\$}_{32r}$, and $\pmb{\$}_{33r}$ can be obtained. Then, the kinematic screws of moving platform $\pmb{\$}_k$, which are $\pmb{\$}_{k1}$, $\pmb{\$}_{k2}$, and $\pmb{\$}_{k3}$, can be calculated.

$$
\begin{cases}
\pmb{\$}_{31r} = [1, 0, 0, 0, -1, -m_1/n_1], \\
\pmb{\$}_{32r} = [0, 1, 0, 0, 0, 0], \\
\pmb{\$}_{33r} = [0, 0, 1, -1, 0, 0],
\end{cases}
$$

$$
\pmb{\$}_k = \begin{cases}
\pmb{\$}_{k1} = [1, 0, 0, 0, 0, 1], \\
\pmb{\$}_{k2} = [0, 1, 0, 1, 0, 0], \\
\pmb{\$}_{k3} = [0, 0, 1, -m_1/n_1, 0, 0].
\end{cases}
\tag{4}
$$

$\pmb{\$}_k$ indicates that 2-UCU/RRR PM has the pure

rotational ability around the x, y, and z axes, which can replace the motion of knee flexion–extension, knee internal–external rotation, and ankle varus–valgus.

3.1.2 Inverse kinematics

The following assumptions are made: The initial location of the moving frame coincides with that of the fixed frame, and its final location can be obtained by a successive rotation of α around the w axis, followed by a

second rotation of β around the displaced u axis, and finally followed by a third rotation of γ around the displaced w axis. Then, the resulting rotation matrix can be derived by Euler angle representation [21–23]. The position vector of p expressed in the fixed frame is assumed $p = [x_p, y_p, z_p]$. In addition, the vectors of A_i and B_i ($i = 1, 2, 3$) with respect to the fixed frame can be expressed.

$$R_B^A = \begin{bmatrix} c\alpha c\gamma - c\beta s\alpha s\gamma & -c\beta c\gamma s\alpha - c\alpha s\gamma & s\alpha s\beta \\ c\gamma s\alpha + c\alpha c\beta s\gamma & c\alpha c\beta c\gamma - s\alpha s\gamma & -c\alpha s\beta \\ s\beta s\gamma & c\gamma s\beta & c\beta \end{bmatrix},$$

$$\begin{cases} a_1 = [-\sqrt{3}a \ 0 \ 0]^T, & b_1^P = [-\sqrt{3}b \ 0 \ 0]^T, \\ a_2 = [\sqrt{3}a \ 0 \ 0]^T, & b_2^P = [\sqrt{3}b \ 0 \ 0]^T, \\ a_3 = [0 \ 3a \ 0]^T, & b_3^P = [0 \ 3b \ 0]^T, \end{cases} \quad (5)$$

where s and c denote sin and cos, respectively.

The loop-closure equation of each limb can be written as follows:

$$a_i + l_i s_i = p + b_i. \quad (6)$$

In Eq. (6), s_i is a unit vector pointing from A_i to B_i. b_i is the vector of the ith limb, which can be derived by $b_i = R_B^A b_i^P$. Furthermore, l_i is the length of the ith limb, but it is a fixed length when $i = 3$. k_{ij} is the unit vector of the jth revolute pair in the ith limb. Figure 8 shows that the revolute axis in vertex A_3 is perpendicular to the third limb at any time. Therefore, taking the dot-product of both sides of Eq. (6) with k_{31}, x_p can be obtained in terms of Eq. (7):

$$(a_3 + l_3 s_3)^T k_{31} = (p + b_3)^T k_{31} = 0. \quad (7)$$

Fig. 8 Diagram of 2-U$\underline{C}$U/R$\underline{R}$R PM.
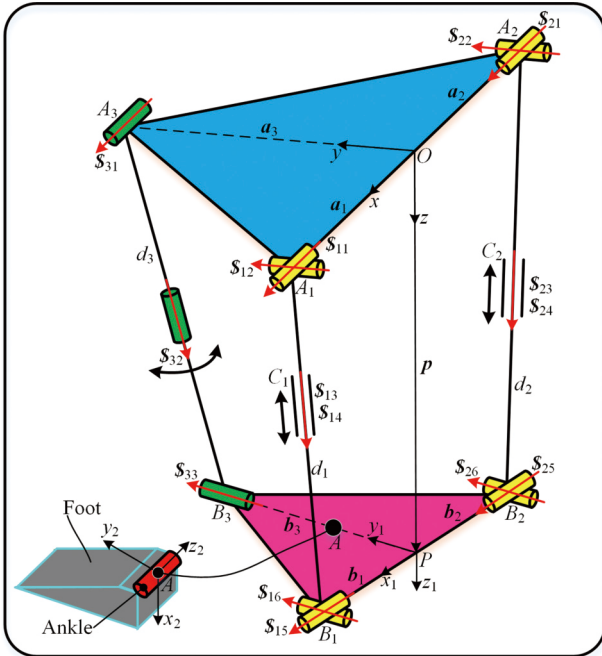
Given that the unit vector of the second revolute pair is perpendicular to the plane $A_1 A_2 B_1 B_2$ at any time and RRR limb has a constant length, the relationships can be obtained as follows:

$$k_{12} \perp (p + b_1), \quad k_{22} \perp (p + b_2), \quad |a_3 - b_3 - p| = l_3. \quad (8)$$

Based on Eqs. (6)–(8), the rotation angle of the moving platform, namely, α, β, and γ, can be determined. Therefore, the inverse solutions of 2-U$\underline{C}$U/RRR PM can be obtained when the values of α, β, and γ are given, that is, the length l_i ($i = 1, 2$) of the ith limb can be calculated:

$$l_i = \sqrt{(a_{i,x} - b_{i,x})^2 + (a_{i,y} - b_{i,y})^2 + (a_{i,z} - b_{i,z})^2}. \quad (9)$$

3.1.3 Dexterity analysis

Jacobian matrix [24–26] plays an important role in the performance analysis of PMs, especially in the investigation of singularity, stiffness, and dexterity. It can be divided into constraint Jacobian matrix and kinematic Jacobian matrix, which can be derived by screw theory [27]. Based on Ref. [28], the fully Jacobian matrix of 2-U$\underline{C}$U/R$\underline{R}$R PM can be obtained:

$$J = \begin{bmatrix} J_{k11} \\ J_{k12} \\ J_{c1} \\ J_{c2} \\ J_{k2} \\ J_{c3} \end{bmatrix} = \begin{bmatrix} (b_1 \times s_{4,1})^T & s_{4,1}^T \\ (b_2 \times s_{4,2})^T & s_{4,2}^T \\ ((b_3 - l_3 s_3) \times s_{1,3})^T & s_{4,2}^T \\ 0 & s_{3,3}^T \\ s_{2,3}^T & 0 \\ (b_3 \times s_{2,3})^T & s_{2,3}^T \end{bmatrix}, \quad \dot{q} = \begin{bmatrix} \dot{l}_1 \\ \dot{l}_2 \\ 0 \\ 0 \\ 0 \\ \dot{\theta}_3 \end{bmatrix}, \quad (10)$$

where J is the fully Jacobian matrix, J_{k11} and J_{k12} are the kinematic Jacobian matrices of two U$\underline{C}$U limbs, J_{k2} is the kinematic Jacobian matrix of R$\underline{R}$R limb, J_{c1}, J_{c2}, and J_{c3} are the constraint Jacobian matrices of R$\underline{R}$R limb, $\dot{l}_1$ and $\dot{l}_2$ are the linear velocities of actuated joint of U$\underline{C}$U, and $\dot{\theta}_3$ is the angular velocity of the actuated joint of R$\underline{R}$R.

The dexterity of 2-U$\underline{C}$U/R$\underline{R}$R PM is used to evaluate whether singularity occurs within the reachable space of the mechanism end-effector as well as verify its kinematic feasibility to be used in transfermoal prosthetic mechanism. Dexterity can be solved in terms of its condition number [29,30] derived by its Jacobian matrix.

$$\kappa(J) = \frac{\lambda_{max}}{\lambda_{min}}, \quad (11)$$

where $\kappa(J)$ is condition number, and λ_{max} and λ_{min} are the maximum and minimum eigenvalues of the Jacobian matrix, respectively.

The average geometric sizes are $l_1 = 375$ mm, $a = 78$ mm, and $b = 75$ mm by measuring the subjects' shanks. Only three special positions when $\gamma = -20°$, $0°$, and $30°$ are considered during the dexterity analysis because the

internal–external rotation of the knee is less used, as shown in Fig. 9.

Therefore, the kinematics of 2-UCU/RRR PM can be used as in the transfemoral prosthetic mechanism and replace the movements of the knee and ankle. Moreover, no singularity is observed within its reachable space, and its condition number is 0−1 when the moving platform is among the range 0° to 90° around the x axis and −20° to 20° around the y axis, which indicates that its kinematic dexterity is good.

3.1.4 Buckling analysis

Buckling analysis is necessary because the axial length of 2-UCU/RRR PM is much larger than its radial length. Its collapse or destruction due to overload can be avoided by evaluating the maximum critical carrying load. According to Refs. [31–33], critical multiplier μ_i under the ith eigenvalue can be calculated by using the Lanczos method [34], and finally the maximum critical carrying load of 2-UCU/RRR in jth case ($j = 1, 2, 3$), which is F_{λ_j},

can be solved according to Ref. [28].

The HTP mechanism is subjected to heavy loads when it acts as the support leg while the sound one is swinging in gait cycle. Moreover, the varus–valgus rotation of the ankle in this state always causes the instability of the human body, and the internal–external rotation of the knee is not activated in the support phase. Thus, only the working conditions when TAs are walking in the sagittal plane are considered.

The ground reaction forces in the sagittal plane are $F_{g1} = \begin{bmatrix} f_{g1}, n_{g1} \end{bmatrix}^T$, $F_{g2} = \begin{bmatrix} f_{g2}, n_{g2} \end{bmatrix}^T$, and $F_{g3} = \begin{bmatrix} f_{g3}, n_{g3} \end{bmatrix}^T$ measured by the 3D force-measuring platform (AMTI), as shown in Fig. 10. The direction of F_{g2} is vertically upward, but the directions of F_{g1} and F_{g3} are upward and their angles are $\varphi_h = \varphi_t = 10°$ in the vertical direction. Moreover, the frictional force between the prosthetic foot and the ground is ignored.

Thus, the loads on the moving platform of 2-UCU/RRR PM can be derived by equilibrium equations and inverse dynamics as follows:
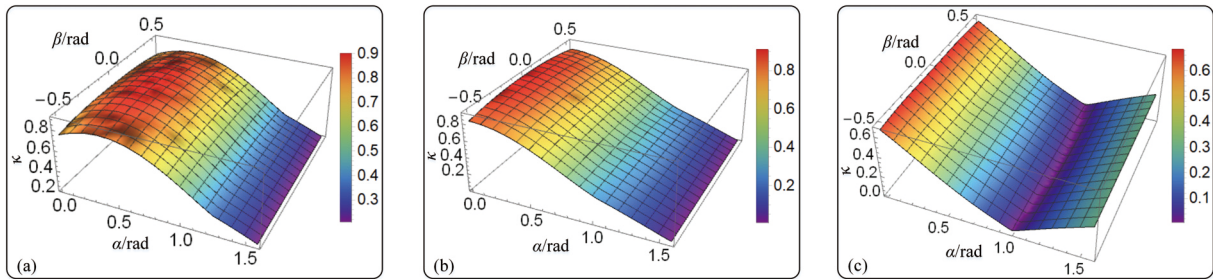

Fig. 9 Dexterity results of 2-UCU/RRR PM: (a) $\gamma = -20°$, (b) $\gamma = 0°$, and (c) $\gamma = 30°$.
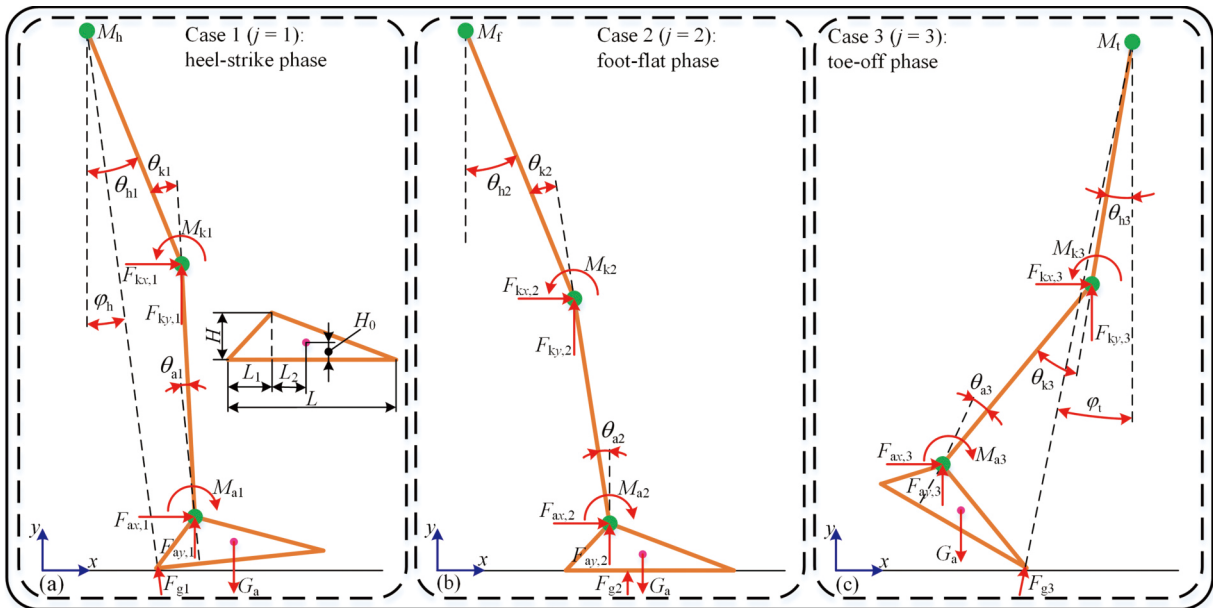

Fig. 10 Mechanical analysis of shank and working conditions of HTP mechanism: (a) Case 1, (b) Case 2, and (c) Case 3.

$$\sum F_{ax,j} = m_a a_{ax,j}, \quad \sum F_{ay,j} = m_a a_{ay,j}, \quad \sum M_j = I_a \alpha_j, \quad (12)$$

where $F_{ax,j}$ and $F_{ay,j}$ are exerted on the ankle joint, which are the resulting forces along the x and y axes, respectively in the jth state case, m_a is the mass of the foot, $a_{ax,j}$ and $a_{ay,j}$ are the acceleration of the foot along the x and y axes, respectively, in the jth state case, M_j is the resulting moment exerted on the ankle joint, I_a is the inertia of the foot, and α_j is the angular acceleration of the foot in the jth state case, which is around the z axis.

3.2 Stability analysis

The stability of the amputees is an important performance when they are walking with the prostheses. Zero moment point (ZMP) [35,36] is an index that can evaluate the stability of the amputees with the lower extremity prostheses in the support phase. It is a point where the horizontal moment component of the amputees' ground reaction force with respect to the ground is zero.

Assume that the ground reaction force and moment on right heel are expressed as $F_g = (f_x, f_y, f_z)^T$ and $T_g = (t_x, t_y, t_z)^T$, respectively. $R_p = (p_x, p_y, p_z)^T$ is the position vector of the center of gravity with respect to ZMP, as shown in Fig. 11. M is the mass located at the center of mass of TAs, $R_m = (x_m, y_m, z_m)^T$ is the position vector of the center of mass with respect to the global coordinate system, R_g is the position vector of the ground reaction force with respect to the ZMP, $E = (E_x, E_y, E_z)^T$ and $L = (L_x, L_y, L_z)^T$ are the total momentum and angular momentum of TAs, respectively, and $g = (0, 0, -g)^T$ is the acceleration of gravity.

Figure 11 shows that the resultant moment of GRF on the right heel with respect to ZMP can be obtained.
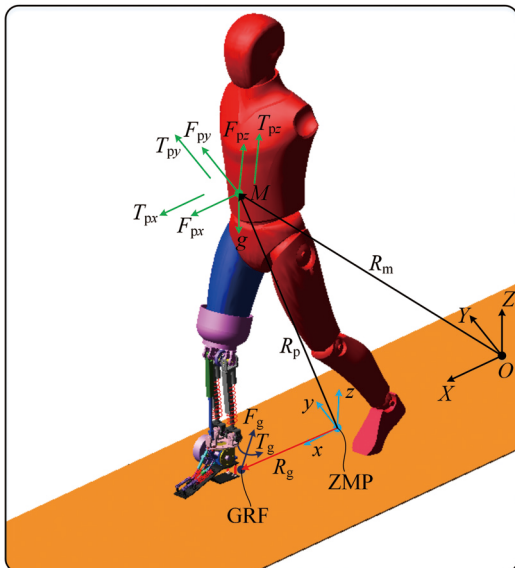

Fig. 11   ZMP based on stable polygon region.

$$T(R_p) = (R_m - R_p + R_g) \times F_g + T_g. \quad (13)$$

Based on the dynamic theory, the following can be obtained:

$$\begin{cases} \dot{E} = Mg + F_g, \\ \dot{L} = R_m \times Mg + T, \end{cases} \quad (14)$$

where F_g and T denote that TAs are subjected to forces and moments in addition to gravity.

Based on Eqs. (13) and (14), the moment subjected on the right heel with respect to point O can be obtained:

$$T(R_p) = \dot{L} - R_m \times Mg + (\dot{E} - Mg) \times R_p. \quad (15)$$

Therefore, the position of ZMP along the x and y directions can be calculated in terms of ZMP theory.

$$p_x = \frac{-\dot{L}_y + \dot{E}_x p_z + Mg x_m}{\dot{E}_z + Mg} = \left(x_m - \frac{z_m \ddot{x}_m}{\ddot{z}_m + g} \right) \cdot \cos \theta_v. \quad (16)$$

where x_m, z_m, $\ddot{x}_m$ and $\ddot{z}_m$ are the spatial position and acceleration of center of mass of human along x and z directions.

Finally, the stability of TAs can be evaluated by analyzing their centroid acceleration and spatial position.

4   Simulations and results

4.1   Human dynamic simulation

Assuming that TAs are walking on the sagittal plane, the motion trajectory of flexion–extension of the knee can be obtained by the curve fitting method.

$$\begin{cases} \alpha_k = \sum_{r=1}^{10} a_r t^{10-r}, \\ \beta_k = 0, \end{cases} \quad (17)$$

where α_k is the rotational angle of the knee flexion–extension, and β_k is the rotational angle of the ankle varus–valgus. $a_1 = 39000$, $a_2 = -190000$, $a_3 = 390000$, $a_4 = -400000$, $a_5 = 230000$, $a_6 = -70000$, $a_7 = 8700$, $a_8 = 760$, $a_9 = -280$, and $a_{10} = -5.9$. t is the gait time variable, which is [0, 1.2 s].

Although the main motion of the knee is flexion–extension in the sagittal plane, by the human anatomy and motion analysis, the existence of internal–external rotation of the knee has a positive effect for a human walking on different roads. Figure 1 shows that the nine-order polynomial function adopted to fit the gait data of the knee internal–external rotation can be obtained:

$$\theta_v = \sum_{k=1}^{10} b_k t^{10-k}, \quad (18)$$

where $b_1 = -13000$, $b_2 = 72000$, $b_3 = -160000$, $b_4 = 190000$, $b_5 = -130000$, $b_6 = 48000$, $b_7 = -8400$, $b_8 = 330$, $b_9 = 37$, and $b_{10} = -0.16$.

Therefore, human dynamic analysis is implemented for TAs with HTP mechanism, and the knee joints' moments and power generation are analyzed.

Compared with the amputees' knee biomechanics, which are presented in Fig. A1(c) and Fig. A2(b), the results in Fig. 12 show that the knee of HTP mechanism has human-like moment and power in the support phase. The knee moment of the HTP mechanism is similar to that of normal subjects, as shown in Fig. 12(a). Although errors exist between the knee moments of the HTP mechanism and the sound leg, they are relatively closer during TA walking, which indicates that the HTP mechanism can be used as prosthesis for TAs, and the dynamic performances of the HTP mechanism conform to the biomechanical characteristics of TAs. The HTP mechanism can generate the required peak power and ensure that the amputees walk smoothly in the support phase, as shown in Fig. 12(b). Moreover, the simulation results of knee biomechanics are closer to the gait experimental data. The existing error may be caused by the rigid connection of the kinematic pairs and the material property of the model.

Compared with the amputees' hip biomechanics presented in Figs. A1(b) and A2(a), the knee biomechanical performances are improved evidently by using the compression springs and WEDC device in the HTP mechanism. Hip biomechanics is also optimized, as shown in Fig. 13. In Fig. 13(a), the residual hip moment is strengthened in the HS and FF phases, and the burden of residual hip is reduced in the TO phase, which will enhance the stability when TAs walking and reduce its excessive energy consumption, as shown in Fig. 13(b).

Except that the motor provides the energy for the designed HTP mechanism when the amputees are walking, the compression springs and WEDC device also play the function of energy generation and transfer, that is, the compression springs absorb energy when the knee flexes and generate energy when the knee extends. On the contrary, the WEDC device absorbs energy when the knee extends and generates energy when the knee flexes. The change of energy absorption and generation of the motor, WEDC device, and compression springs is shown in Fig. 14, and their detailed parameters are expressed in Table 4.

Table 4 shows that due to the energy absorption and generation of the WEDC device and compression springs, as well as the partial energy transfer, the required peak power of the motor is lower than that of normal subjects from 137.05 to 94.74 W when the prosthesis lifts off the ground.
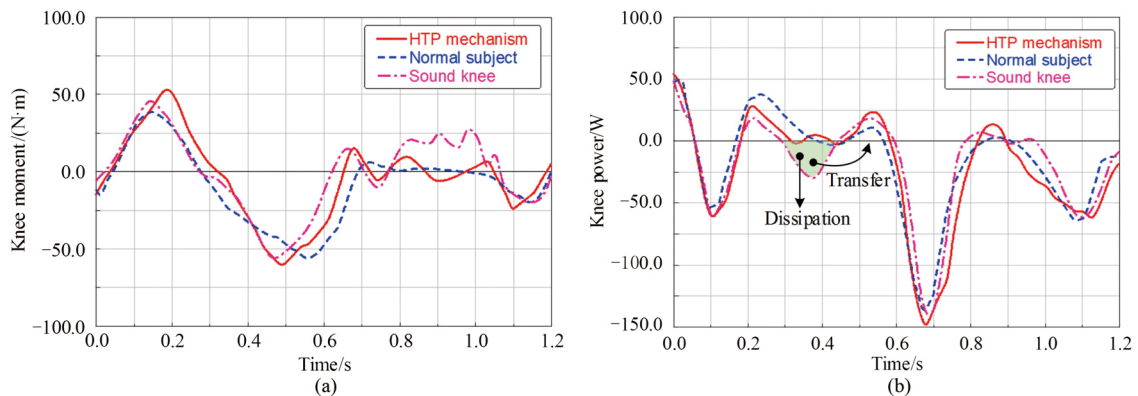

Fig. 12 Knee biomechanics of the amputees with HTP mechanism: (a) knee moments and (b) knee power.
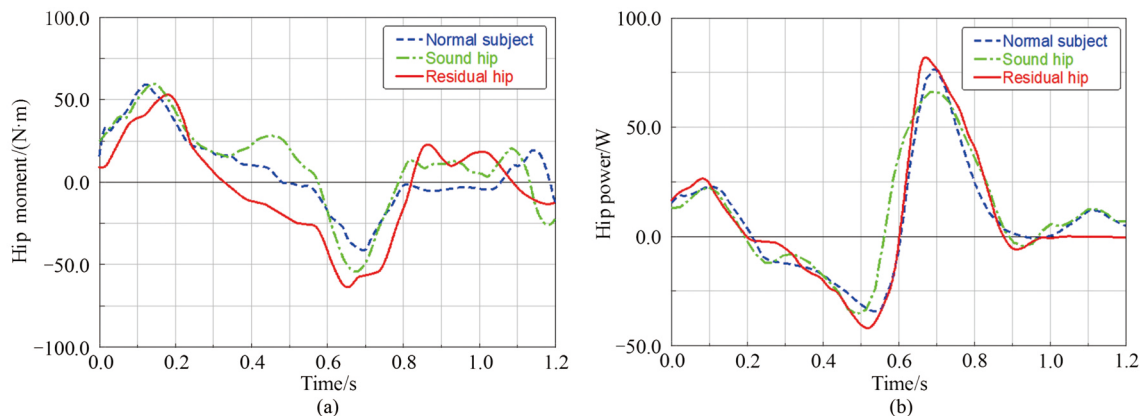

Fig. 13 Hip biomechanics of amputees with HTP mechanism: (a) hip moments and (b) hip power.

4.2 Load-bearing capacity

The foot average parameters are m_a = 1.2 kg, I_a = 0.01 kg·m^2, L = 250 mm, H = 90 mm, H_0 = $H/2$, L_1 = 65 mm, and L_2 = $L/2-L_1$. The motion parameters of foot can be obtained by the previous gait experimental test, as shown in Table 5.

For the three cases, the working conditions of the HTP mechanism can be obtained by the above derivation, as shown in Table 6. In addition, its boundary condition is the fixed base of 2-U$\underline{C}$U/R$\underline{R}$R PM installed on the socket.

The buckling analysis results of 2-U$\underline{C}$U/R$\underline{R}$R PM can be obtained by the finite element method, and its maximum deformation trend under critical unstable state is presented in Fig. 15.
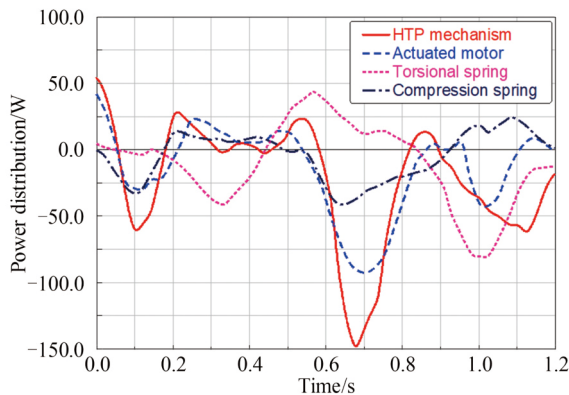
Furthermore, the maximum critical carrying load of

Fig. 14 Power contribution results of energy devices in HTP mechanism.

Table 4 Peak power contribution of energy devices in HTP mechanism during walking (unit: W)

Phases	Normal subject	Total	Motor	Compression spring	WEDC device
Heel-strike	49.21	54.08	41.84	0.00	4.81
Foot-flat	−52.30	−60.31	−29.35	−32.44	−3.59
Heel-off	37.50	28.22	22.70	0.00	−39.76
Toe-off	−137.05	−147.60	−94.74	−40.89	43.60

Table 5 Motion parameters of foot

Gait phase	Motion	Value
Heel-strike phase (Case 1)	$a_{ax,1}$	−4.59 m/s^2
	$a_{ay,1}$	−1.26 m/s^2
	$\alpha_{az,1}$	3.23 rad/s^2
Foot-flat phase (Case 2)	$a_{ax,2}$	0 m/s^2
	$a_{ay,2}$	0 m/s^2
	$\alpha_{az,2}$	0 rad/s^2
Toe-off phase (Case 3)	$a_{ax,3}$	17.63 m/s^2
	$a_{ay,3}$	6.14 m/s^2
	$\alpha_{az,3}$	−49.16 rad/s^2

Table 6 Working conditions of HTP mechanism

Heel-strike phase		Foot-flat phase		Toe-off phase	
Loads	Value	Load	Value	Load	Value
$F_{g1,x}$	−96.47 N	$F_{g2,x}$	0.00 N	$F_{g3,x}$	131.40 N
$F_{g1,y}$	780.00 N	$F_{g2,y}$	595.00 N	$F_{g3,y}$	780.00 N
$F_{ax,1}$	129.94 N	$F_{ax,2}$	0.00 N	$F_{ax,3}$	−114.29 N
$F_{ay,1}$	−769.66 N	$F_{ay,2}$	−595.00 N	$F_{ay,3}$	−760.78 N
$M_{az,1}$	48.96 N/m	$M_{az,2}$	−23.80 N/m	$M_{az,3}$	−121.68 N/m

2-U$\underline{C}$U/R$\underline{R}$R PM in the HS, FF, and TO phases can be obtained, as shown in Table 7.

Upon closer investigation of the results, the critical multipliers in the HS, FF, and TO phases are all greater than 1, which denotes that 2-U$\underline{C}$U/R$\underline{R}$R PM has sufficient carrying capacity and will not be unstable in normal gait cycle. The maximum bearing capacity of 2-U$\underline{C}$U/R$\underline{R}$R PM is approximately 2534.7 N, that is, it can bear another 178.47 kg weight in addition to TAs' weight.

4.3 Stability verification

The average foot length of the selected subjects is approximately 255 mm. Thus, its steady position range along the x axis is [−127.5 mm, 127.5 mm]. Through the human dynamic analysis, the centroid acceleration and spatial position of TAs with HTP mechanism can be calculated, as shown in Fig. 16(a).

Therefore, the ZMP position of TAs with HTP mechanism along the x direction can be determined in terms of Eq. (16), as shown in Fig. 16(b). Figure 16(b) shows the improvement effect of knee internal–external rotation on the stability when the human is walking on the ground.

The HTP mechanism does not have the motion characteristics of knee internal–external rotation, and the maximum ZMP position, which is closer to the critical boundary of instability, along the x axis is approximately 112.38 mm when TAs are walking in the TO phase. The maximum ZMP position along the x axis is approximately 92.95 mm in the HO phase when TAs are walking with the motion characteristic of internal–external rotation. Owing to the adaptive compensation caused by knee internal–external rotation, the knee flexion–extension of HTP mechanism will be less disturbed in the HO phase when the human is walking but still assisted by the compression springs embedded in prismatic pairs, which will lead to a slight instability for the HTP mechanism. However, the inertia of the center of gravity of the human body from the HO phase to the TO phase effectively compensates for this instability in the HO phase. Thus, the ZMP position becomes large in this phase but still within the stability area, and the ZMP position moves toward the center of the stable region, which indicates the good adaptive stability of the HTP mechanism with the motion characteristics of knee internal–external rotation.
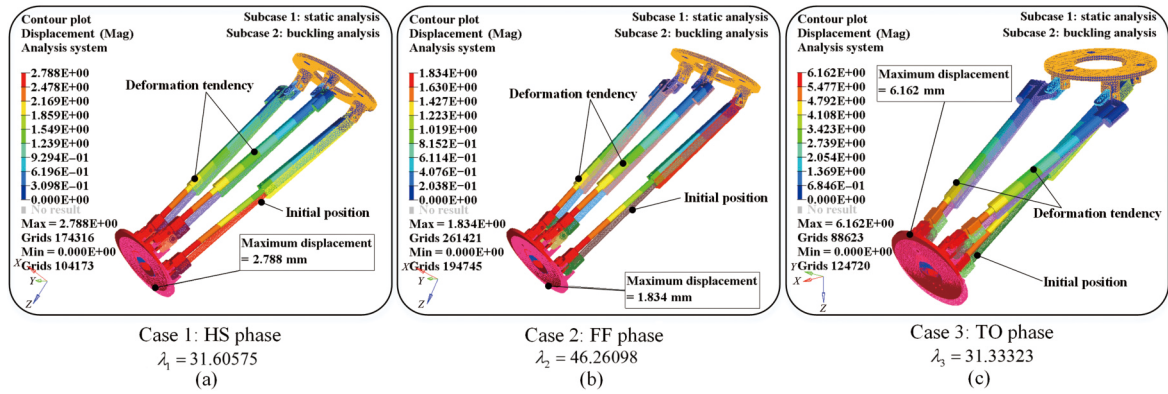
Fig. 15 Buckling analysis result of 2-U$\underline{C}$U/R$\underline{R}$R mechanism (unit: mm): (a) HS phase, (b) FF phase, and (c) TO phase.

Table 7 Carrying capability of 2-U$\underline{C}$U/R$\underline{R}$R PM

Gait phase	Critical factors, λ_j	Critical load, F_{λ_j}/N
Heel-strike phase	3.61	2815.8
Foot-flat phase	4.26	2534.7
Toe-off phase	3.33	2597.4

4.4 Multimode motion

According to the human dynamic analysis, the feasibility of HTP mechanism has been verified and can be used for TAs. Moreover, the designed HTP mechanism has the multimode motion to overcome or adapt to uneven roads, as shown in Fig. 17.
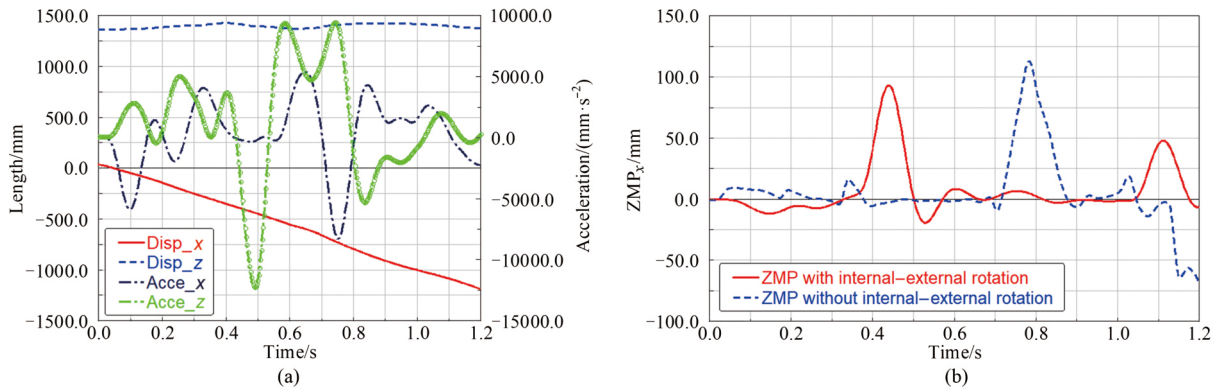

Fig. 16 Stability result of TAs with HTP mechanism: (a) acceleration and spatial position and (b) ZMP position along x axis. Disp: displacement, Acce: acceleration.
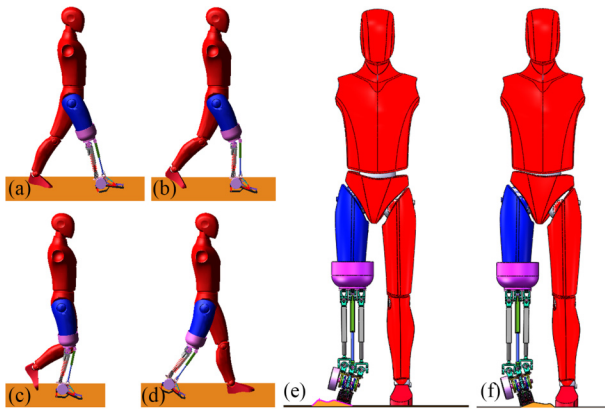

Fig. 17 Multimode motion of HTP mechanism: (a) knee flexes in HS phase, (b) knee flexes in FF phase, (c) knee flexes in HO phase, (d) knee flexes in TO phase, (e) ankle valgus, and (f) ankle varus.

The HTP mechanism addresses the problem that the existing transfemoral prosthetic mechanism can only move in the sagittal plane. It improves more kinematic possibility for TAs within the same time dimension.

5 Conclusions

Transfemoral prosthetic configurations are synthesized based on the human lower-extremity kinesiology, and a series–parallel HTP mechanism, which is composed of an ankle–foot prosthetic mechanism and a PM of three-DoF rotation, is proposed. Then, Lie group theory is adopted to synthesize the configurations of PM, and 2-U$\underline{C}$U/R$\underline{R}$R PM is determined for use in the proposed prosthetic mechanism. The motion feasibility of 2-U$\underline{C}$U/R$\underline{R}$R PM is verified by its inverse kinematics and dexterity based on

the full Jacobian matrix. Its bearing capacity is also analyzed based on buckling analysis so that it can safely support the human body. A gait-based wearable clutched energy device is proposed and used in the knee joint, which can provide energy for knee stance flexion so that the leg can lift from the ground easily, and can impede the leg's velocity in knee SW extension for the next HS phase of gait. By co-operating with the springs in the prismatic pairs, the clutched device can make the prosthetic mechanism have the ability of energy recycling along with the gait rhythm of knee and lower energy consumption under human-like motion as well as improve its biomechanical performances.

In conclusion, the usage of PM in transfemoral prosthetic mechanism can make the prosthetic mechanism have human-like motion functions, simplifying its mechanical structure, and achieving light weight under better bearing capacity. In future works, the coupled relationship between skeletal muscles and joints motion will be explored to develop the electromyography control system in the designed prosthetic mechanism, and its prototype will be manufactured to verify the design correctness.

Nomenclature

Abbreviations

DoF	Degree-of-freedom
FF	Foot-flat
GRF	Ground reaction force
HO	Heel-off
HS	Heel-strike
HTP	Hybrid transfemoral prosthetic
PM	Parallel mechanism
SW	Swing
TA	Transfemoral amputee
TO	Toe-off
TO-I	Toe-off I
TO-II	Toe-off II
WEDC	Wearable energy-damper clutched
ZMP	Zero moment point

Variables

$a_{ax,j}$, $a_{ay,j}$	Acceleration of the foot along the x- and y-axis, respectively
$a_{i,x}$, $b_{i,x}$	x component element of points A_i and B_i in fixed frame, respectively ($i = 1, 2$)
$a_{i,y}$, $b_{i,y}$	y component element of point A_i and B_i in fixed frame, respectively ($i = 1, 2$)
$a_{i,z}$, $b_{i,z}$	z component element of point A_i and B_i in fixed frame, respectively ($i = 1, 2$)

$\boldsymbol{a}_i$	Position vector of A_i with respect to the fixed frame
A	Rotational angle around w-axis in w-u-w Euler angles ($i = 1, 2, 3$)
B	Rotational angle around u'-axis in w-u-w Euler angles
$\boldsymbol{b}_i$	Position vector of B_i with respect to the fixed frame ($i = 1, 2, 3$)
$\boldsymbol{b}_i^{\mathrm{P}}$	Position vector of B_i with respect to the moving frame ($i = 1, 2, 3$)
$C(\rho_j, t)$	Energy function is the optimization objective
d_{ci}	Compressed distances of ith prismatic pairs ($i = 1, 2$)
$\boldsymbol{E}$	Total momentum of TAs
$F_{ax,j}$, $F_{ay,j}$	Resulting forces along the x and y axes in the jth state case, respectively
F_{cfi}	Elastic forces generated by the compression springs ($i = 1, 2$)
$\boldsymbol{f}_{gi}$	Force components of $\boldsymbol{F}_{gi}$ in heel-strike, foot-flat and toe-off phases ($i = 1, 2, 3$)
$\boldsymbol{F}_g$	Ground reaction force on right heel
$\boldsymbol{F}_{gi}$	Ground reaction force in heel-strike, foot-flat and toe-off phases ($i = 1, 2, 3$)
g	Gravitational acceleration
$\boldsymbol{g} = (0, 0, -g)^{\mathrm{T}}$	Gravitational acceleration vector
I_a	Inertia of the foot
$\boldsymbol{J}$	Fully Jacobian matrix
$\boldsymbol{J}_{k1n}$	Kinematic Jacobian matrices of the nth U$\underline{\mathrm{C}}$U limbs ($n = 1, 2$)
$\boldsymbol{J}_{cm}$	mth constraint Jacobian matrices of R$\underline{\mathrm{R}}$R limbs ($m = 1, 2, 3$)
$\boldsymbol{J}_{k2}$	Kinematic Jacobian matrices of R$\underline{\mathrm{R}}$R limbs
k_{fi}	ith compression springs' stiffness ($i = 1, 2$)
k_e	Torsion spring's stiffness
$\boldsymbol{k}_{ij}$	Unit vector of the jth revolute pair in the ith limb
l_i	Length of the ith limb ($i = 1, 2$)
$\dot{l}_i$	Linear velocities of actuated joint in U$\underline{\mathrm{C}}$U limbs ($i = 1, 2$)
$\boldsymbol{L}$	Total angular momentum of TAs
M_j	Resulting moment exerted on the ankle joint
ΔM_{ph1}	Lack of hip flexor moment in the prosthetic system
ΔM_{ph2}	Extra hip extensor moment which endured by the transfemoral amputees
ΔM_{pk1}	Lack of knee extensor moment in the prosthetic system
ΔM_{pk2}	Lack of knee flexor moment in the prosthetic system
ΔM_{pk3}	Redundant knee extensor moment in the prosthetic system
$\boldsymbol{n}_{gi}$	Moment components of $\boldsymbol{F}_{gi}$ in heel-strike, foot-flat, and toe-off phases ($i = 1, 2, 3$)
p_x	Position of ZMP in x direction
$\boldsymbol{p}$	Position vector of the origin of moving frame with respect to the fixed frame
$\boldsymbol{R}_B^A$	Transformation matrix from moving frame to the fixed frame
$\boldsymbol{R}_g$	Position vector of the ground reaction force with respect to the ZMP
$\boldsymbol{R}_m$	Position vector of the center of mass with respect to the global frame

$\boldsymbol{R}_p$	Position vector of the center of gravity with respect to ZMP
$\boldsymbol{s}_i$	Unit vector pointing along A_iB_i ($i = 1, 2, 3$)
$\boldsymbol{s}_{j,i}$	Unit vector of the jth joint in the ith limb ($i = 1, 2$ and $j = 1, 2, \ldots, 6$; $i = 3$ and $j = 1, 2, 3$)
$T(\rho_j, t)$	Knee moment generated by optimized torsion spring
$\boldsymbol{T}_g$	Moments generated from ground reaction force on right heel
$T(\boldsymbol{R}_p)$	Resultant moment of GRF on the right heel with respect to ZMP
V	Optimized volumes
V^*	Desired volumes
$x_m, \ddot{x}_m$	Spatial position and acceleration of center of mass of human along x axis
$z_m, \ddot{z}_m$	Spatial position and acceleration of center of mass of human along z axis
α_j	Angular acceleration of the foot around z axis in the jth state case
α_k	Rotational angle of the knee flexion–extension,
β_k	Rotational angle of the ankle varus–valgus
$\lambda_{\max}, \lambda_{\min}$	Maximum and minimum eigenvalues of the fully Jacobian matrix, respectively
ρ_j	Design variable
$\rho_{\min}$	Minimum density of the element to avoid the optimization singularity
$\kappa(\boldsymbol{J})$	Condition number
$\theta(t)$	Knee extension angle
$\dot{\theta}(t)$	Angular acceleration
$\dot{\theta}_3$	Angular velocity of the actuated joint of R<u>R</u>R limb
θ_v	Knee internal–external rotation angle
$\Delta\theta_{kf1}$	Knee flexion increment in stance phase
$\Delta\theta_{kf2}$	Difference between maximum plantar flexion and maximum dorsiflexion of ankle
$\Delta\theta_{ke}$	Knee extension angle increment in stance phase (here $\Delta\theta_{ke} = \Delta\theta_{ke1}$ in Fig. 1)
$\Delta\theta_{ke}(t)$	Knee extension angle threshold
Ω	Design area
Γ	Rotational angle around w''-axis in w-u-w Euler Angles
$\boldsymbol{\$}_{ij}$	jth kinematic screws in the ith limb ($i = 1, j = 1, 2, \ldots, 6$)
$\boldsymbol{\$}_{3j}$	jth kinematic screws in the 3rd limb ($j = 1, 2, 3$)
$\boldsymbol{\$}_{3jr}$	jth constraint screws in the 3rd limb ($j = 1, 2, 3$)
$\boldsymbol{\$}_k$	Kinematic screws set of moving platform
$\boldsymbol{\$}_{kj}$	jth kinematic screw element in $\boldsymbol{\$}_k$ ($j = 1, 2, 3$)

Appendix   Spring stiffness determination

A   Biomechanics of human lower extremity

The able-bodied lower extremity will not collapse in the support phase because the sum of net muscle moments generated by the hip, knee, and ankle is positive, as shown in Figs. A1(b)–A1(d). Moments and power of TAs are referred to Refs. [37–42], and that of the able-bodied are tested in our laboratory, as shown in Figs. A1 and A2.

Currently, linear elastic devices are used in prosthetic mechanisms to improve their biomechanical behavior and mechanical performances, but uncoordinated gait patterns and high metabolic consumption always occur. Moreover, these devices do not consider the relationship between movement-energetic requirements of the hip and knee of the amputated and able-bodied legs. As a resolution to these difficulties, the proposed WEDC device can effectively improve the human–machine biomechanical behaviors in the HTP mechanism.

Compared with able-bodied subjects, with the absence of power generation of the knee, the hip and knee moments of the amputated leg are ΔM_{ph1} and ΔM_{pk1} less in the HS phase, respectively, and ΔM_{ph2} and ΔM_{pk2} less in the FF phase, respectively, which will increase the risk of instability for TAs and limit their movement. Moreover, the knee moment of amputated legs is ΔM_{pk3} less in the TO phases. At this time, the hip moment increases ΔM_{ph3} to help TAs avoid the difficulty in lifting their amputated leg from the ground at the expense of high metabolic consumption, as shown in Fig. A2(a). Generally, the net joint moment of the amputated legs is clearly insufficient for TAs in the support phase, and the support duration is shortened by approximately 0.2 s, which will increase the burden of their sound legs.

The torsion spring, similar to the quadricep femoris, stores the elastic energy in knee stance extension and releases to facilitate knee flexion in the TO phase, and assists the leg to lift off from the ground, but it does not work in knee stance flexion. Moreover, it can slow down the swing velocity of the leg in knee swing extension for the next HS phase of gait, which can be regarded as a damper. Oppositely, a compression spring, similar to the gastrocnemius and bicep femoris muscle, is built into the cylinder of U<u>C</u>U limb, stores energy in knee stance flexion, and releases them in knee stance extension to assist the center of gravity of human body upward movement.
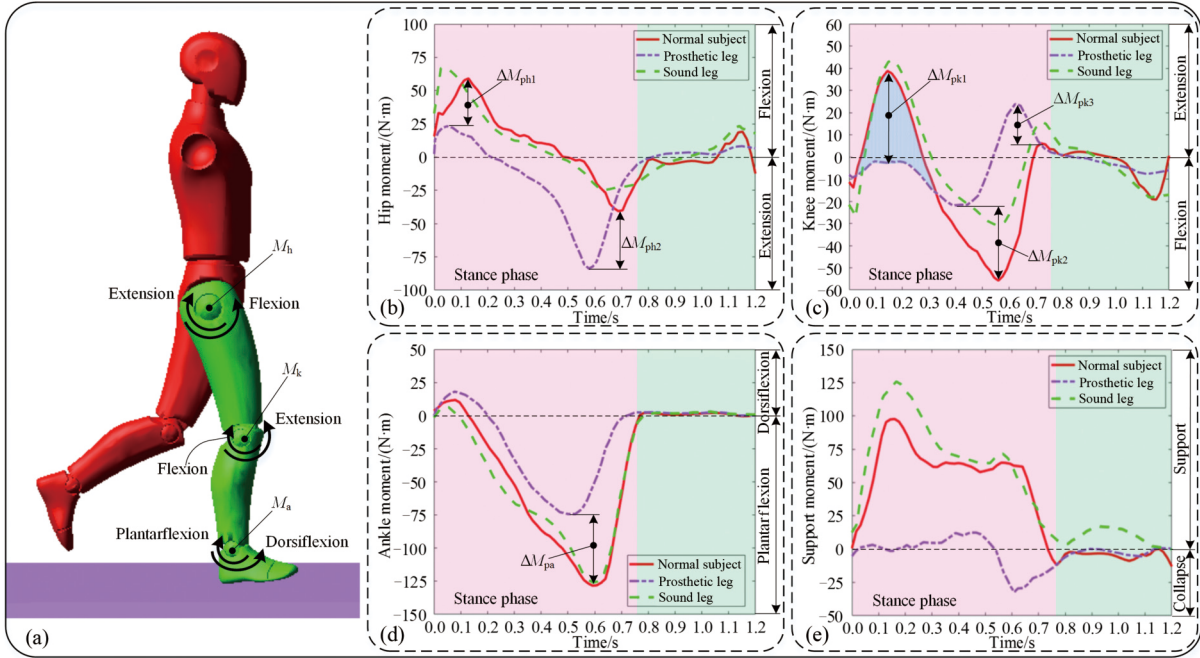
Fig. A1 Moment comparison between normal subjects' right legs, prosthetic and sound legs of the transfemoral amputees. (a) Human support phase; (b) hip moments; (c) knee moments; (d) ankle moments; and (e) support moments.
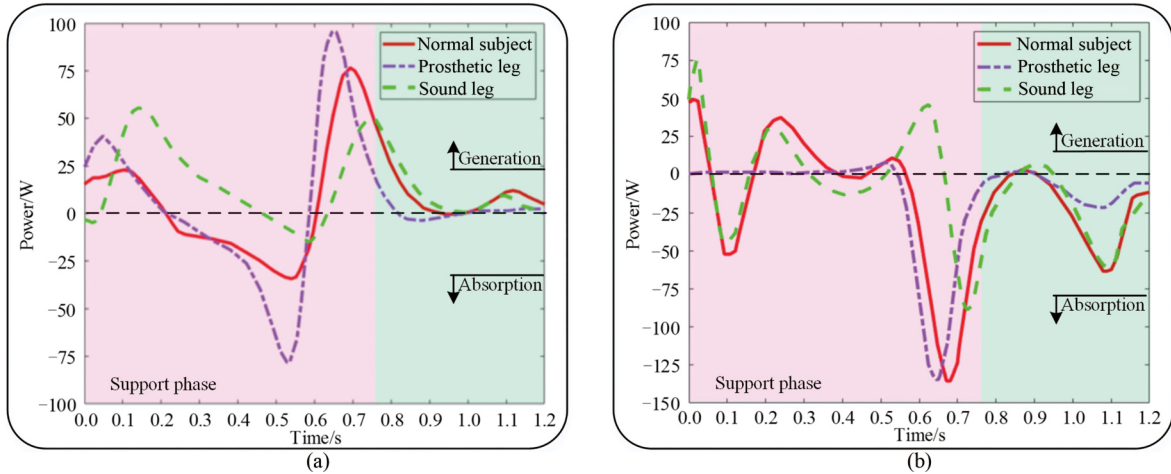

Fig. A2 Power of the hip and knee versus gait cycle. (a) Hip and (b) knee.

B Compression spring stiffness

Assuming that the knee flexes with θ_{kf1} and θ_{kf2}, respectively, in the gait cycle when TAs are walking, the compressed distances of prismatic pairs are d_{c1} and d_{c2} as obtained by inverse kinematics. The elastic forces and moments generated by the springs can be calculated.

$$F_{cf1}(\theta_{kf1}, t) = k_{f1} \cdot d_{c1}, \quad F_{cf2}(\theta_{kf2}, t) = k_{f2} \cdot d_{c2}. \quad (A1)$$

$$(\Delta M_{ph1} + \Delta M_{pk1}) = \sqrt{3} F_{cf1} \cdot \sin(0.5\pi - \theta_{kf1}) \cdot a,$$
$$\Delta M_{pk3} = \sqrt{3} F_{cf2} \cdot \sin(0.5\pi - \theta_{kf2}) \cdot a. \quad (A2)$$

The compression springs' stiffness can be calculated by Eqs. (A1) and (A2), and $k_{f1} = 10.41$ N/mm and $k_{f2} =$ 33.93 N/mm. Thus, the spring stiffness in the prismatic pairs is selected as $k_f = k_{f2} \approx 34$ N/mm.

C Torsional spring

The WEDC device only works in knee extension, the push rod rotates clockwise with the rotational wheel, and the push rod turns the ratchet together, as shown in Fig. A2(a). At this moment, the torsion spring has stored ΔM_{ph2} and ΔM_{pk2} of moments associated with $\Delta\theta_{ke}$ of the knee stance extension, which compensate for the lack of hip and knee moments. The required stiffness coefficient of the customized torsion spring can be calculated.

$$(\Delta M_{ph2} + \Delta M_{pk2}) = k_e \cdot \Delta\theta_{ke}. \qquad (A3)$$

Therefore, the stiffness coefficient of the torsion spring can be calculated, and $k_e \approx 213.8062$ N·m/rad.

References

1. Ziegler-Graham K, MacKenzie E J, Ephraim P L, et al. Estimating the prevalence of limb loss in the United States: 2005 to 2050. Archives of Physical Medicine and Rehabilitation, 2008, 89(3): 422–429

2. Ngan C C, Andrysek J. Modeling and design of the automatic stance phase lock (ASPL) knee joint control mechanism for paediatric users with transfemoral amputations. IEEE Transactions on Neural Systems and Rehabilitation Engineering, 2020, 28(1): 203–210

3. Sup F, Bohara A, Goldfarb M. Design and control of a powered transfemoral prosthesis. International Journal of Robotics Research, 2008, 27(2): 263–273

4. Yang U J, Kim J Y. Mechanical design of powered prosthetic leg and walking pattern generation based on motion capture data. Advanced Robotics, 2015, 29(16): 1061–1079

5. Lenzi T, Cempini M, Hargrove L, et al. Design, development and testing of a lightweight hybrid robotic knee prosthesis. International Journal of Robotics Research, 2018, 37(8): 953–976

6. Lawson B E, Varol H A, Goldfarb M. Standing stability enhancement with an intelligent powered transfemoral prosthesis. IEEE Transactions on Biomedical Engineering, 2011, 58(9): 2617–2624

7. Wang Y, Yu J J, Pei X. Fast forward kinematics algorithm for real-time and high-precision control of the 3-RPS parallel mechanism. Frontiers of Mechanical Engineering, 2018, 13(3): 368–375

8. Russo M, Herrero S, Altuzarra O, et al. Kinematic analysis and multi-objective optimization of a 3-UPR parallel mechanism for a robotic leg. Mechanism and Machine Theory, 2018, 120: 192–202

9. Moosavian A, Xi F F. Holonomic under-actuation of parallel robots with topological reconfiguration. Mechanism and Machine Theory, 2016, 96: 290–307

10. Song M J, Guo S, Qu H B, et al. China Patent, ZL201910438441.2, 2020-10-09

11. Hisano G, Hashizume S, Kobayashi Y, et al. Factors associated with a risk of prosthetic knee buckling during walking in unilateral transfemoral amputees. Gait & Posture, 2020, 77: 69–74

12. Yu J J, Liu X J, Ding X L. Mathematical Foundation of Mechanisms and Robotics. 2nd ed. Beijing: China Machine Press, 2016, 11–78 (in Chinese)

13. Chhabra R, Emami M R. A generalized exponential formula for forward and differential kinematics of open-chain multi-body systems. Mechanism and Machine Theory, 2014, 73: 61–75

14. Bendsoe M P, Sigmund O. Topology Optimization: Theory, Methods and Applications. 2nd ed. Berlin Heidelberg: Springer-Verlag, 2004, 1–68

15. Xie X D, Wang S T, Ye M, et al. Isogeometric topology optimization based on energy penalization for symmetric structure. Frontiers of Mechanical Engineering, 2020, 15(1): 100–122

16. Sigmund O, Maute K. Topology optimization approaches: a comparative review. Structural and Multidisciplinary Optimization, 2013, 48(6): 1031–1055

17. Zhu B L, Zhang X M, Zhang H C, et al. Design of compliant mechanisms using continuum topology optimization: a review. Mechanism and Machine Theory, 2020, 143: 103622

18. Stolpe M, Svanberg K. An alternative interpolation scheme for minimum compliance topology optimization. Structural and Multidisciplinary Optimization, 2001, 22(2): 116–124

19. Huang Z, Zhao Y S, Zhao T S. Advanced Spatial Mechanism. Beijing: Higher Education Press, 2006, 19–39 (in Chinese)

20. Laus L P, Simas H, Martins D. Machine efficiency determined using graph and screw theories with application in robotics. Mechanism and Machine Theory, 2020, 148: 103748

21. Tasi L W. Robot Analysis: The Mechanics of Serial and Parallel Manipulators. New York: Wiley, 1999, 116–259

22. Tsai L W, Joshi S. Kinematic analysis of 3-DOF position mechanisms for use in hybrid kinematic machines. Journal of Mechanical Design, 2002, 124(2): 245–253

23. Wang L P, Xu H Y, Guan L W, et al. A novel 3-PUU parallel mechanism and its kinematic issues. Robotics and Computer-Integrated Manufacturing, 2016, 42: 86–102

24. Rezaei A, Akbarzadeh A, Nia P M, et al. Position, Jacobian and workspace analysis of a 3-PSP spatial parallel manipulator. Robotics and Computer-integrated Manufacturing, 2013, 29(4): 158–173

25. Sun T, Lian B B, Yang S F, et al. Kinematic calibration of serial and parallel robots based on finite and instantaneous screw theory. IEEE Transactions on Robotics, 2020, 36(3): 816–834

26. Joshi S, Tsai L W. Jacobian analysis of limited-DOF parallel manipulators. Journal of Mechanical Design, 2002, 124(2): 254–258

27. Choi H B, Ryu J. Singularity analysis of a four degree-of-freedom parallel manipulator based on an expanded 6×6 Jacobian matrix. Mechanism and Machine Theory, 2012, 57: 51–61

28. Song M J, Guo S, Wang X Y, et al. Dynamic analysis and performance verification of a novel hip prosthetic mechanism. Chinese Journal of Mechanical Engineering, 2020, 33(1): 17

29. Herrero S, Pinto C, Altuzarra O, et al. Analysis of the 2PRU-1PRS 3DOF parallel manipulator: kinematics, singularities and dynamics. Robotics and Computer-Integrated Manufacturing, 2018, 51: 63–72

30. Arsenault M, Boudreau R. Synthesis of planar parallel mechanisms while considering workspace, dexterity, stiffness and singularity avoidance. Journal of Mechanical Design, 2006, 128(1): 69–78

31. Farrokh M, Afzali M, Carrera E. Mechanical and thermal buckling loads of rectangular FG plates by using higher-order unified formulation. Mechanics of Advanced Materials and Structures, 2021, 28(6): 608–617

32. Kulkarni K, Singh B N, Maiti D K. Analytical solution for bending and buckling analysis of functionally graded plates using inverse trigonometric shear deformation theory. Composite Structures, 2015, 134: 147–157

33. Shen J J, Wadee M A, Sadowski A J. Interactive buckling in long thin-walled rectangular hollow section struts. International Journal of Non-linear Mechanics, 2017, 89: 43–58

34. Radau L, Gerzen N, Barthold F J. Sensitivity of structural response in context of linear and non-linear buckling analysis with solid shell finite elements. Structural and Multidisciplinary Optimization, 2017, 55(6): 2259–2283

35. Dijkstra E J, Gutierrez-Farewik E M. Computation of ground reaction force using zero moment point. Journal of Biomechanics, 2015, 48(14): 3776–3781

36. Oh S E, Choi A, Mun J H. Prediction of ground reaction forces during gait based on kinematics and a neural network model. Journal of Biomechanics, 2013, 46(14): 2372–2380

37. Seroussi R E, Gitter A, Czerniecki J M, et al. Mechanical work adaptations of above-knee amputee ambulation. Archives of Physical Medicine and Rehabilitation, 1996, 77(11): 1209–1214

38. Winter D A. Energy generation and absorption at the ankle and knee during fast, natural, and slow cadences. Clinical Orthopaedics and Related Research, 1983, 175: 147–154

39. Winter D A. Biomechanics and Motor Control of Human Movement. 2nd ed. Waterloo: University of Waterloo Press, 1990

40. Millard M, Emonds A L, Harant M, et al. A reduced muscle model and planar musculoskeletal model fit for the simulation of whole-body movements. Journal of Biomechanics, 2019, 89(24): 11–20

41. Winter D A. Overall principle of lower-limb support during stance phase of gait. Journal of Biomechanics, 1980, 13(11): 923–927

42. Donelan J M, Kram R, Kuo A D. Simultaneous positive and negative external mechanical work in human walking. Journal of Biomechanics, 2002, 35(1): 117–124